Available online at www.sciencedirect.com
SCIENCE DIRECT
Remote Sensing of Environment 102 (2006) 237–249
Remote Sensing of Environment
www.elsevier.com/locate/rse

Improved detection of turbid waters from ocean color sensors information

Andre Morel *, Simon Bélanger

Laboratoire d'Océanographie de Villefranche (CNRS and Université P. & M. Curie) B.P. 08, 06238 Villefranche-sur-mer, France

Received 16 September 2005; received in revised form 23 January 2006; accepted 26 January 2006

Abstract

Various empirical techniques have been developed to identify turbid marine waters within satellite ocean color imageries. The present technique, which essentially rests on the enhancement of reflectance in the green part of the spectrum when sediments are present, accounts for the improved knowledge regarding the relationship between the chlorophyll concentration and the scattering coefficient in oceanic case-1 waters. It also accounts for the bidirectional character of the light field emerging from a water body and thus for the sensitivity of the water-leaving radiance to the observational conditions (viewing angle and sun angle). Therefore, the thresholds, above which the turbid waters can be detected, are not constant. They depend on the chlorophyll concentration and on geometry (on the zenith-sun angle). The practical way of implementing such a discriminating tool is explained. Examples of the application of this technique are provided for level-2 and level-3 satellite data (SeaWiFS and MERIS).

Keywords: Ocean color; Coastal zone; Turbidity quantification; Suspended particulate matter threshold

1. Introduction and motivations

The ocean color imagery, as routinely processed by several space agencies, often shows a red color – a color encoding attributed to very high chlorophyll concentration (Chl) – along many coasts of the world ocean and particularly in semi-enclosed seas. Even if there are some good reasons to expect sizeable enhancements of the algal biomass in these shallow zones (because of a possible nutrient influx from terrestrial origin, and/or rapid recycling of nutrients), it is also known that the algorithms (of the blue-to-green ratio type) developed for case-1 waters (Morel & Prieur, 1977) fail in such zones, with the result of strongly overestimating (Chl). Often, these coastal areas are influenced by mineral sediments, brought by rivers or stirred up from the bottom, as well as by colored dissolved organic matter of terrestrial origin (CDOM or Gelbstoff or yellow substance). As a result, these waters belong to case-2 waters, either sediment-dominated (case-2S) or yellow substance dominated (case-2Y) waters, with all intermediate possible combinations. Specific techniques and algorithms (review and references in IOCCG, 2000; see also Maritorena et al., 2002) attempt to extract from the remotely sensed data three independent components, namely S, Y, and (Chl), the sediment concentration, the yellow substance concentration, and the chlorophyll concentration, respectively. With a less ambitious aim, a tool (or "flag") is needed by which the "turbid" case-2S waters can be easily and accurately identified to warn of misestimate of (Chl). In addition, this flag can also delineate the turbid zones and provide temporal monitoring of the offshore sediment extent, through the use of an excess of turbidity index.

Actually, such a tool has already been developed for the Coastal Zone Color Scanner (CZCS) imagery (Bricaud & Morel, 1987). It was based on the observation that the reflectance in the green part of the spectrum (namely at 550 nm with the CZCS) is "anomalously" heightened in sediment loaded waters, when compared to that of case-1 waters, which would have the same (Chl) (Fig. 1 in Bricaud & Morel, 1987). The cause of this increase, as well as the reason for the correlative failure of current (Chl)-algorithms, deserves some detailed examination.

The field database, on which the empirical criterion developed by Bricaud and Morel (ibid.) rested, is now

* Corresponding author.
E-mail address: morel@obs-vlfr.fr (A. Morel).

0034-4257/$ - see front matter © 2006 Elsevier Inc. All rights reserved.
doi:10.1016/j.rse.2006.01.022

considerably increased in number and quality. This improved knowledge allows the anomalous reflectance to be better defined and thus the criterion to be refined. Other important phenomena related to the bidirectional character of the upward radiance field were previously ignored, while it is presently realized that they impact the reflectance threshold which ultimately fixes the criterion. Therefore, the aim of the present study is to account for both these new field data and theoretical findings, and then, by relying on a revised semi-analytical bio-optical model (Morel & Maritorena, 2001), to develop a sound technique to be used with modern and more sensitive ocean color sensors.

2. Theoretical background

2.1. The basic equations

After the atmospheric correction has been performed, the marine signal, commonly called the water-leaving radiance (L_w), is extracted from the total signal as measured by the satellite at the top of the atmosphere (wavelength dependency is omitted in the following equations). In what follows, it will be admitted that the atmospheric correction can be made accurately (this proviso will be relaxed thereafter).

The water-leaving radiance, $L_w(\theta_v)$, directed toward the sensor (θ_v is the viewing angle, from the pixel toward the sensor) originates from an in-water upward radiance, $L_u(\theta')$, where θ' is the nadir angle, which is related to θ_v through Snell's law ($\sin\theta_v = 1.34\sin\theta'$). Besides its dependency on the water optical properties (the ultimate goal of remote sensing), L_w also depends on the observation geometry, which is defined by θ', by the azimuth difference between the solar plane and the plane of observation, denoted $\Delta\varphi$, and by the illumination conditions, to first order determined by the zenith-sun angle, θ_s. Actually, for a given sun's position, the in-water illumination conditions also depend on the sea state (governed by the wind speed module, W), and on the relative proportions of diffuse sky radiation and direct solar radiation, which in turn depend on the aerosol content (depicted by the aerosol optical thickness, τ_a), and aerosol composition. For the sake of simplification, the arguments τ_a and W are nonetheless omitted in what follows.

Conveniently, $L_w(\theta_s, \theta_v, \Delta\varphi)$ is transformed into the "normalized water-leaving radiance" (Gordon & Clark, 1981), denoted $[L_w]_N$. This normalization is obtained by dividing the measured (actually the retrieved) radiance by the downward irradiance just above the surface, $E_d(0^+)$, and then by re-mutiplying it by the solar irradiance, F_0, at the top of the atmosphere and for a mean sun–earth distance, so that

$$[L_w]_N = [L_w/E_d(0^+)]F_0 \quad (1)$$

In remote sensing applications, $E_d(0^+)$ is not measured, but rather computed as

$$E_d(0^+) = F_0 \varepsilon t_d(\theta_s)\cos(\theta_s) \quad (1')$$

where t_d is the diffuse transmittance of the atmosphere and ε accounts for the varying sun–earth distance ($\varepsilon = d^{-2}$, where d is the actual distance expressed in astronomical unit). The normalization through Eq. (1), however, does not remove the dependency upon the geometrical conditions of satellite observation. By accounting for this dependency and introducing the $F_0/E_d(0^+)$ ratio, Eq. (1) becomes

$$[L_w]_N(\theta_s, \theta_v, \Delta\varphi) = L_w(\theta_s, \theta_v, \Delta\varphi)/\varepsilon t_d(\theta_s)\cos(\theta_s) \quad (1'')$$

The irradiance reflectance of a water body just beneath the surface (denoted 0^-) is defined as the ratio of upward irradiance to downward irradiance, both at 0^-

$$R(0^-) = E_u(0^-)/E_d(0^-) \quad (2)$$

This reflectance essentially depends on the water optical properties (see below) and also on the illumination conditions, summarized by θ_s. It is related to the normalized water-leaving radiance through (see, e.g., Morel & Gentili, 1996; Morel & Mueller, 2002)

$$[L_w]_N(\theta_s, \theta_v, \Delta\varphi) = R(0^-, 0_s)F_0\Re(\theta_v, W)/Q(\theta_s, \theta', \Delta\varphi) \quad (3)$$

where $\Re$ is a dimensionless quantity, which merges all the effects of reflection and refraction at the air/sea interface. From an initial value (0.529 when $\theta_v = 0$ and for seawater refractive index equal to 1.34), $\Re$ is essentially constant as long as $\theta_v < 40°$; then, it starts to decrease and becomes slightly wind-dependent (Gordon, 2005). The varying quantity $Q(\theta_s, \theta', \Delta\varphi)$ (unit: sr) relates any slant upward radiance to the upward irradiance (both beneath the surface) through

$$L_u(0^-, \theta', \theta_s, \Delta\varphi) = E_u(0^-)/Q(\theta', \theta_s, \Delta\varphi) \quad (4)$$

In summary, after due geometric corrections (involving Q and $\Re$), the (normalized) radiances emerging from the water body can be expressed via Eq. (3), as a function of R. This reflectance is the fundamental quantity to the extent that it can be related to the optical properties of the water body (and therefore to the substances in it). All the above quantities actually are wavelength-dependent, even if λ was not introduced in the previous equations, in which emphasis was put on geometric considerations and bidirectional effects.

The physical interpretation of reflectance (an apparent optical property, AOP, sensu Preisendorfer, 1961) consists of relating the spectral irradiance reflectance, $R(\lambda)$, to relevant inherent optical properties (IOP) of the medium, namely the absorption and the backscattering coefficients, $a(\lambda)$ and $b_b(\lambda)$, respectively. This operational relationship writes

$$R(\lambda, \theta_s) = f'[b_b(\lambda)/(b_b(\lambda) + a(\lambda))] \quad (5)$$

where f' cannot be a constant, which would mean that R is an IOP. Actually, this number is sensitive to the directionality of the incident illumination (namely on θ_s, but not exclusively, as τ_a and W, at least in principle, intervene). For a given illumination condition, f' is also depending on the IOPs and, as a consequence, on the wavelength. In case-1 waters, the dependence on IOPs can be replaced by a dependence on (Chl), to the extent that in such waters these optical properties are (by definition) related only to the chlorophyll concentration. The core of the following discussion is the variations in the ratio of the inherent optical coefficients (b_b and a, in Eq. (5)) as a

function of (Chl) and the possible deviations in presence of sediment.

2.2. Differences between case-1 waters and turbid case-2 waters

In case-1 waters, the variations in $b_b(\lambda)$ and $a(\lambda)$ can be related to the bio-optical state of the water, itself empirically indexed on (Chl) (see, e.g., Morel & Maritorena, 2001, thereafter denoted MM-01). As a consequence of the adoption of average relationships between $b_b(\lambda)$ or $a(\lambda)$, and (Chl), $R(\lambda)$ can also be modeled as a function of (Chl). In the same way, any ratio of two reflectances, $R(\lambda_1)/R(\lambda_2)$, at two wavelengths ($\lambda_1$ and λ_2) in the visible range, can also be expressed as a function of (Chl). Such ratios are the basis of semi-analytical algorithms in use for case-1 waters, which are known as "blue-to-green ratio" techniques. Note that purely empirical algorithms also make use of these ratios (e.g., the OC4V4 algorithm for SeaWiFS, O'Reilly et al., 1998). These ratios (with λ_1=443, 490, or 510 nm, and $\lambda_2 \approx 560$ nm) steadily decrease for increasing (Chl) (see Fig. 11 in the above reference). In case-2 waters, the situation is quite different. Mean relationships indexed on (Chl) do no longer exist, because of the presence of other optically significant materials (Y and S) which do not co-vary with (Chl). Yellow substance-dominated and sediment-dominated case-2 waters behave differently, as briefly reviewed below.

In case-2Y waters, the cause of departure from case-1 waters lies in the additional absorption by colored dissolved material (yellow substance or Gelbstoff). This substance produces a strong (exponential) increase in absorption toward the shorter wavelengths. Such waters appear darker than case-1 waters having the same (Chl), because $R(\lambda)$ is depressed (Eq. (5)), particularly in the short wavelength domain where this additional absorption may become dominant. Therefore, any blue-to-green ratio technique, applied without care, necessarily leads to an overestimate of (Chl). The identification of these waters is not examined here.

In case-2S waters, the optical change results essentially from the presence of additional particles, mainly of mineral nature, and hereafter collectively called sediments. The straightforward consequence of their presence is an increase in scattering and in backscattering. These particles are often weakly colored (reddish, brownish) and thus contribute to enhance the absorption coefficient, in particular in the short wavelength domain (see Babin et al., 2003b). Nevertheless, in as much as this effect on absorption remains small compared to that on scattering, R is definitely enhanced, as commonly observed in milky turbid coastal waters. This increased reflectance, which affects the whole spectral domain, is better detected within the spectral domain where absorption is at its minimum; therefore, the green part of the spectrum (around 560 nm) a priori is the best candidate for the detection of the enhancement, because the sediment absorption is weak, and the algal and yellow substance absorptions are here minimal. These considerations were the rationale of the criterion adopted by Bricaud and Morel (1987) for a sensitive discrimination between case-1 and turbid case-2 waters (actually they used the wavelength 550 nm, available with the CZCS sensor). If a sharp discrimination is not aimed at, and rather a rough mapping of the zones with high sediment concentration is the main goal, wavelengths from the green to the near-infrared, can be equivalently used, as done, for instance for AVHRR (Stumpf & Pennock, 1989), for SPOT, (Doxaran et al., 2002), or for MERIS (Moore et al., 1999).

In case-1 waters, the amount of particles (algal and associated non-algal particles) increases along with the chlorophyll concentration, in a more or less regular manner. As a consequence, the particle scattering coefficient, b_p (at λ=550 nm) increases for increasing (Chl). The empirical relationship between both quantities has been found to be a non-linear one, according to the generic empirical expression given in Gordon and Morel (1983)

$$b_p(550) = B[\mathrm{Chl}]^E \tag{6}$$

where the exponent E was found to be about 0.62, and B, on average, was 0.3, with an upper limit B_{max} reaching 0.45. Above this upper limit, the waters enter into the turbid case-2S category. Introducing the above relationship (Eq. (6)), with its upper limit (actually B_{max} was set at 0.50 instead of 0.45), into the reflectance model of Morel (1988) provided the upper reflectance value, $R_{lim}(550)$, which was adopted by Bricaud and Morel (1987). This upper value, which slightly varies with (Chl) (cf. Fig. 1 in the above reference), was used as a threshold to identify the turbid waters in ocean color (CZCS) imagery. Actually, an alternative criterion making use of another wavelength (namely 510 nm) can also be proposed and will be examined later on.

2.3. The failure of the blue-to-green algorithm in presence of sediment

A simple reasoning can be made under the assumption of linearity by expressing R according to

$$R(\lambda) = f\, b_b(\lambda)/a(\lambda)$$

Note that the factor f differs from f' in Eq. (5) (see discussion in Loisel & Morel, 2001). It is worthwhile at this point to recall that a blue-to-green band ratio algorithm is represented by a $R(\lambda_1)/R(\lambda_2)$ ratio (with $\lambda_1 < \lambda_2$),

$$R(\lambda_1)/R(\lambda_2) = [b_b(\lambda_1)/b_b(\lambda_2)]/[a(\lambda_2)/a(\lambda_1)]$$

Such a ratio steadily decreases when (Chl) increases (e.g., O'Reilly et al., 1998).

We suppose now that b_b is increased by Δb_b because of the presence of additional particles (or the presence of particles with a higher backscattering efficiency, $\tilde{b}_b$, as expected for mineral particles) . If, in addition, we assume that these particles are not absorbing (so that the ratio $a(\lambda_2)/a(\lambda_1)$ remains unchanged, but see later) and they scatter light in a neutral fashion (Δb_b constant regardless of the wavelength), the blue-to-green $R(\lambda_1)/R(\lambda_2)$ ratio will evolve as the ratio

$$[b_b(\lambda_1) + \Delta b_b]/[b_b(\lambda_2) + \Delta b_b]$$

The initial $b_b(\lambda_1)/b_b(\lambda_2)$ ratio (before addition of particles) is generally above 1 for most of the chlorophyll range (note that, if molecular backscattering dominates, its value is close to $(\lambda_1/\lambda_2)^{-4.3}$). When adding, and then increasing Δb_b, the above ratio tends toward unity. Therefore, the band ratio algorithm will decrease and fail by returning an overestimated (Chl) value. At extremely high (Chl), the initial $b_b(\lambda_1)/b_b(\lambda_2)$ ratio may be below 1 (this situation may happens because the scattering and backscattering coefficients of phytoplankton are depressed in the blue absorption band—see, e.g., Ahn et al., 1992). In such exceptional cases, the evolution is reversed, and the failure leads to an underestimate of (Chl). This effect is also to be combined with another one, as explained below.

The scattering increase actually induces an increase in K_d (the attenuation coefficient for downward irradiance) and therefore a reduction of the penetration depth $Z_{90}=1/K_d$ (Gordon & McCluney, 1975; this depth, Z_{90}, corresponds to the thickness of that layer from which 90% of the photons forming the upward radiance field originate). As the photons have penetrated less deep before being returned upward, the effect of absorption (in the green) is diminished. The fraction of green photons able to emerge is thus increased, which leads to a spectral shift (as visual observations tell us). Abundant bubbles for instance (Stramski & Tegowski, 2001; Zhang et al., 2004) or non-colored detached liths (from coccolithophorids) dramatically transform a deep-blue sea into a bright turquoise sea, simply because of this effect. In passing, a shallow bottom with reflecting white sand induces the same color shift. In terms of algorithms, such "greener" reflectances are necessarily interpreted as waters having a higher (Chl) than actually they do have.

When considering the actual mineral sediments and detritus in coastal waters, the ideal situation described above is modified. Indeed, these particles, beside of being efficient scatterers, are, as said before, weakly colored. Their regularly increasing absorption toward the shorter wavelengths is well described by an exponential function with a slope around $-0.012\,\mathrm{nm}^{-1}$ (Babin et al., 2003b; Bowers et al., 1996; Roesler et al., 1989). Such a relative increase in blue absorption, compared to green absorption, obviously translates again into an apparent enhancement of (Chl) when a color ratio algorithm, only valid for case-1 waters, is applied. It is worth adding that the simultaneous presence of Gelbstoff with also an exponentially increasing absorption toward the blue (with a steeper slope) reinforces the depression of the blue reflectance, diminishes the $a(\lambda_2)/a(\lambda_1)$ ratio, and thus heightens the (Chl) overestimate.

3. Identifying the turbid waters

3.1. Refining the previous criterion

It can be refined at the light of new field data and modeling studies. The relationship between the scattering coefficient and (Chl) in case-1 waters was recently re-examined on the basis of a much larger dataset, also more homogeneous regarding the analytical methods (Loisel & Morel, 1998). The data restricted to the upper layer as "seen" by a remote sensor are displayed in Fig. 1, together with the average relationship. Transferred to the wavelength 560 nm (by using a λ^{-1} law), this relationship becomes (MM-01)

$$b_p(560) = 0.41[\mathrm{Chl}]^{0.766} \quad (7)$$

The scatter in the distribution of the data in Fig. 1 leads to adopt as upper limit for b_p,

$$b_p(560) = 0.69[\mathrm{Chl}]^{0.766} \quad (7')$$

This relationship is to be introduced into the bio-optical model to produce the limiting $R_{lim}(560)$ values as a function of (Chl). The bio-optical model used for that is that of Morel and Maritorena (2001). Its previous limitation in the domain of high (Chl) has been removed and its applicability extended to $\mathrm{Chl}=10\,\mathrm{mg\,m}^{-3}$ (Morel et al., 2002). These models account for a particle backscattering efficiency, $\tilde{b}_b$, which is made varying with (Chl) and thus allows b to be transformed into b_b (via $b_b=\tilde{b}_b b$). The dependence of $R(560)$ upon the solar position (in a blue sky) is accounted for through the sun-dependent $f'(560)$ coefficient (Eq. (5)). This coefficient is tabulated as a function of θ_s and (Chl). The $R(560, \theta_s, \mathrm{Chl})$ values, as modeled for average case-1 water conditions, and the $R_{lim}(560, \theta_s, \mathrm{Chl})$ values, as modeled by using the upper limit condition (Eq. (7′)), are graphically shown (Fig. 2) (available over the Internet, at oceane.obs-vlfr.fr, directory pub/morel/Rthreshold). Compared with the unique curve (Fig. 1 in Bricaud & Morel, 1987, reproduced in Fig. 2), the family of the present curves demonstrates the sensitivity of the criterion on the solar angle, which was previously ignored. Also a serious difference occurs,

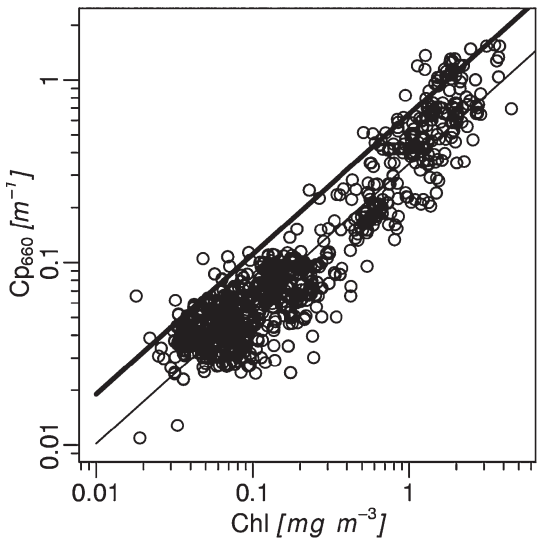

Fig. 1. Particle attenuation coefficient at 660 nm, $c_p(660)$ and chlorophyll concentration, as simultaneously determined within the upper homogeneous layer and in case-1 waters only. This log–log plot is a partial reproduction of Fig. 3 in Loisel and Morel (1998). Note that c_p is practically equal to the particle scattering coefficient, b_p (c_p may exceed b_p by 3% at the most). The thin line represents the average relationship $b_p(660)=0.347[\mathrm{Chl}]^{0.766}$, as given in the above reference; the bold line represents the adopted upper limit for case-1 waters, namely $b_p(660)\approx 0.59[\mathrm{Chl}]^{0.766}$, which leads to Eq. (7′) (at 560 nm).

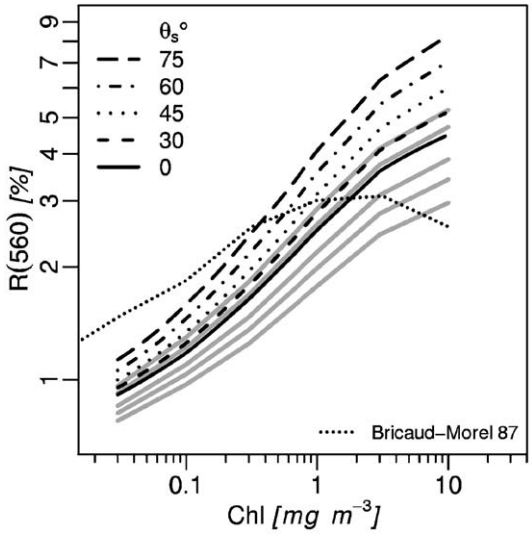

Fig. 2. Log–log plot of irradiance reflectance at 560 nm, $R(560)$, as a function of (Chl), and for various solar zenith angle, θ_s, as indicated. The gray curves represent the result of the bio-optical model when operated with the average case-1 water scattering coefficient (increasing θ_s, from the lower to the upper curve) and the black curves when it is operated with the upper limit (the $b_p(560)$ in Eq. (7′)).These curves are the sun-dependent threshold above which waters are classified as "turbid". Note that $R(560)$ under overcast skies behave as if the sun was at about 45° in a blue sky. The sun-independent threshold (at 550 nm) previously proposed by Bricaud and Morel (1987) is shown for comparison.

particularly in the domain of high (Chl) (>2 mg m^{-3}), which results from the use of the improved (MM-01) bio-optical model.

3.2. Adding an alternative criterion

The reflectance around 510–520 nm seems to be rather insensitive to the chlorophyll concentration in case-1 waters. This "hinge" point was already noted (Clarke et al., 1970) and explained by Duntley et al. (1974). It has been experimentally confirmed, as well as reproduced by models for case-1 waters (e.g., Fig. 8 in Morel & Maritorena, 2001). Note that this approximate stability in reflectance at 510 nm (a MERIS channel) is also used in view of identifying absorbing aerosols (Antoine & Morel, 1999). Fig. 3A, similar to Fig. 2, displays the average and the upper limit values, $R(510, \theta_s, \text{Chl})$ and $R_{lim}(510, \theta_s, \text{Chl})$. The upper limit is obtained by using

$$b_p(510) = 0.63[\text{Chl}]^{0.766} \qquad (7'')$$

Actually, $R_{lim}(510, \theta_s, \text{Chl})$ is not strictly constant; it slightly increases, by a factor of about 1.7, when (Chl) increases from 0.03 to 5–10 mg m^{-3}. This dependency, however, is notably smaller than that of $R_{lim}(560, \theta_s, \text{Chl})$, which increases by a factor of about 5 within the same (Chl) range. Such a lesser dependency may bring some practical advantages, when (Chl) cannot be ascertained (see later). In contrast, the dependency on (Chl) over the same (Chl) range is much larger (actually by a factor 15) at the wavelength 670 nm, now adopted for the turbid water flag for SeaWiFS (starting with the fourth reprocessing). This flag makes use of a constant threshold, $R_{rs}(670) > 0.0012$ sr^{-1} (Robinson et al., 2003), where R_{rs} is the remote sensing reflectance, i.e., $L_w/E_d(0^+)$, and is related to R through (e.g., Morel & Mueller, 2002)

$$R = (1/\Re)Q(\theta', \theta_s, \Delta\varphi)R_{rs}$$

where $\Re$, the term merging all reflection and refraction effects, is equal to 0.529 (Gordon, 2005), and the $Q(670)$ factor varies only with (Chl) and θ_s (when assuming that the water-leaving radiance L_w is emerging from nadir, so that θ' and $\Delta\varphi = 0$). Therefore, in correspondence to the constant threshold value ($R_{rs} = 0.0012$ sr^{-1}), the threshold value, when expressed in terms of R, slightly increases with increasing (Chl) and θ_s values (upper three curves in Fig. 3B). The large differences observed in this figure shows that the turbid 670-flag is lax for many turbid waters (when (Chl) is below 3 mg m^{-3}), which cannot be identified as such.

3.3. Validating the thresholds

Reflectance spectra at null depth are derived from the spectral determinations of upward and downward irradiances (Eq. (2)). Such $E_u(\lambda)$ and $E_d(\lambda)$ measurements have been carried

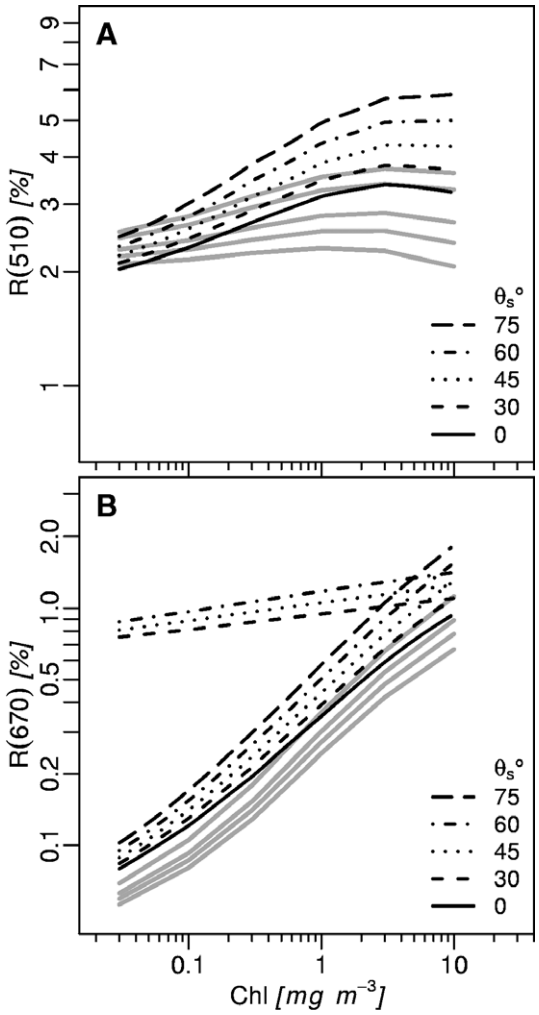

Fig. 3. As for Fig. 3, but for the wavelength 510 nm, and 670 nm (panels A and B, respectively).

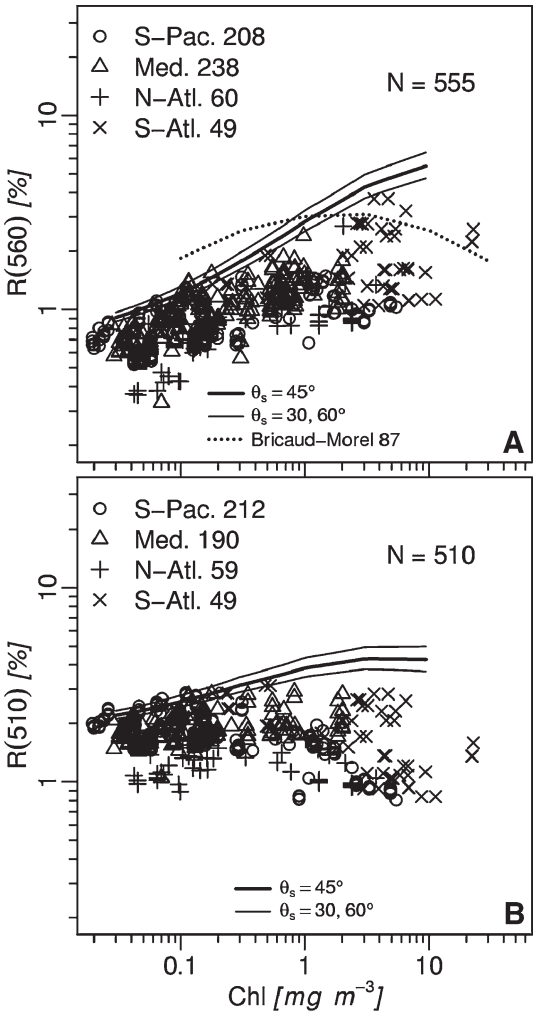

Fig. 4. (A) Irradiance reflectance at 560 nm as a function of (Chl). The three curves are reproduced from Fig. 2 and correspond to the upper limit for θ_s=30, 45, and 60°. The Bricaud-Morel threshold (cf. Fig. 2) is also reproduced. Field data below this curve were all obtained in case-1 waters, namely in South Pacific (Olipac, Paciprod, and Biosope cruises), North Atlantic (Eumeli, Prosope, and Coastlooc-Atl), South Atlantic (Bencal cruise), and Mediterranean Sea. The highest (Chl) values were observed in upwelling areas (Benguela, Morocco, Mauritania, and Peru). All data were obtained with high solar elevations (tropical zones and experiments around the solar noon). Note that, if the Bricaud-Morel threshold is used, five data at high (Chl) migrate into the "turbid" water category. (B) As for (C), but for the wavelength 510 nm and with the upper limit curve from Fig. 3 (θ_s=45°).

out during several cruises in open ocean, and all in case-1 waters (see Table 1 in MM-01). Data acquired during four recent cruises, also in case-1 waters, have been added, namely COAST*l*OOC-cruise 1, from Biscay Bay to Canary Islands, Almofront-2 in the Alboran Sea, PROSOPE in the Moroccan upwelling zone and the Mediterranean sea, BENCAL in the Benguela upwelling ecosystem, BIOSOPE in SE Pacific (1997, 1998, 1999, 2002, and 2004, respectively). Also added are the results of regular surveys at the site where the BOUSSOLE buoy is deployed (Ligurian Sea). The *R*(560) and *R*(510) values as observed during these cruises are plotted as a function of (Chl) (Figs. 4A, and 4B, respectively).

High turbidity resulting from wind induced resuspension of sediment was observed along the coast of Mauritania inside the 50-m isobath (Morel, 1982). Various, mostly turbid, coastal waters around Europe were studied in the frame of the COAST*l*OOC Program, which included six campaigns during the 1997–1998–1999 period, in the North Sea and English channel, Baltic Sea, and in the extended plumes of the Loire, Seine, Thames, Humber, Rhine, and Elbe Rivers, as well as in the Northern Adriatic Sea near the Pô and Adige river mouths (Babin et al., 2003a). Previous data from Rhone river plume (FosBerre cruise, 1977) are also added. The corresponding *R*(560) and *R*(510) values are shown in Fig. 5A and B, respectively.

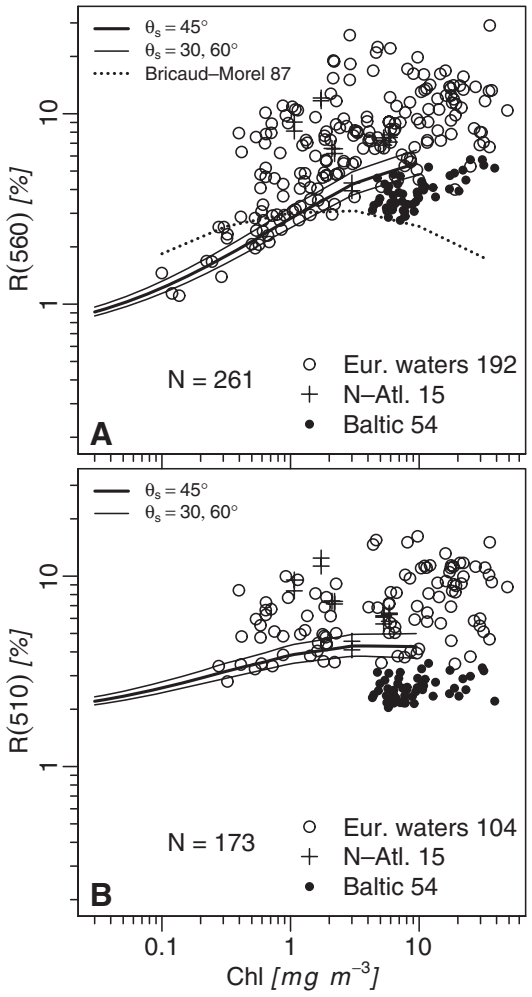

Fig. 5. (A) Irradiance reflectance at 560 nm as a function of (Chl). The three curves (from Fig. 2) correspond to the upper limit for θ_s=30, 45, and 60°. Field data were all obtained in case-2 waters, often under overcast skies, or with θ_s between 30° and 50° for partially cloudy or clear skies (50° to 70° in Baltic Sea). These data (from Northwest African coast and other European waters) are above the upper limit, except those from Baltic Sea (typical of case-2Y waters), which systematically stand below. Note that all the Baltic waters are classified as 'turbid' when using the Bricaud-Morel threshold, whereas a few more (at low (Chl) values) remain inside case-1 water category. (B) As for (A), but for the wavelength 510 nm and with the upper limit curve from Fig. 3 (θ_s=45°). Note that, due to a failure in the equipment, some data (from Adriatic Sea and North Sea) are missing at 510 nm, although they were obtained at 560 nm. Most of these data (in A and B) originate from the COAST*l*OOC program dedicated to coastal waters (see Babin et al., 2003a, 2003b).

For both wavelengths, the distribution of the data with respect to the upper limits of reflectance confirms the reliability of the adopted criteria to discriminate the two types of water. Turbid case-2 and case-1 waters are systematically above and below the thresholds. The wide scatter of the points for case-2S waters is expected as turbidity and (Chl) are not correlated. The particular position of the Baltic Sea data (case-2Y waters) with regards to the upper limit curve is a clear illustration of the impact on reflectance (even at 510 nm) of a very high yellow substance concentration associated with a moderate sediment concentration (Babin et al., 2003a).

Even if lesser, the scatter of the points for case-1 waters is notable (no exclusion was exerted). It obviously may reflect some experimental inaccuracies and differing solar angles. For its major part, however, the observed scatter results from the natural optical variability, which exists within case-1 waters when indexed on the sole (Chl) parameter.

4. Application of the criteria

4.1. Numerical aspects

The ways of expressing and normalizing the water-leaving radiances differ according to agencies and instruments. The practical use of the present threshold will be successively examined for the data provided by three different sensors.

For *SeaWiFS and MODIS*, the products as distributed by the DAAC (Distributed Active Archive Centre) are the normalized water-leaving radiance (Eq. (1)). The introduction of $R_{\mathrm{lim}}(\lambda, \theta_s, \mathrm{Chl})$ into Eq. (3) (with $\lambda = 510$ or 560 nm) allows the high reflectance pixels to be identified as case-2S waters as soon as the inequality below is satisfied

$$[L_w(\lambda)]_N(\theta_s, \theta_v, \Delta\varphi) > [L_w(\lambda)]_{N,\mathrm{lim}}(\theta_s, \theta_v, \Delta\varphi, \lambda)$$

where the limiting value is

$$[L_w(\lambda)]_{N,\mathrm{lim}}(\theta_s, \theta_v, \Delta\varphi) = R_{\mathrm{lim}}(\lambda, \mathrm{Chl}, \theta_s) F_0(\lambda) \Re(\theta_v, W) / Q(\theta_s, \theta_v, \Delta\varphi, \mathrm{Chl}, \lambda) \quad (8)$$

Actually, the SeaWiFS channel is not located at 560 nm but at 555 nm. The modification of $B_{\max}$ (in Eq. (7′)) and therefore of the threshold is minute (<1%) and can be safely neglected. The varying Q factor mainly depends on θ_s the sun zenith angle (Fig. 13.8 in Morel & Mueller, 2002). It also increases (by 25–30%) with increasing (Chl) within the domain of low concentration, from 0.03 to 1 mg m^{-3} (certainly infrequent in case-2S waters); then, for higher (Chl) values, ranging from 1 to 10 mg m^{-3}, Q increases only by about 10–15%. Therefore, a first guess of (Chl) is necessary to enter the appropriate lookup table (Q-LUT, see below).

It has been previously noted that in turbid case-2 waters, the retrieval of (Chl) is generally invalid (actually overestimated). This overestimated value, used as a first guess, will lead to a slight overestimate of both R_{lim} and the Q factor (numerator and denominator in Eq. (8)). These uncertainties have a minor impact when using Eq. (8). If the (invalid) retrieved (Chl) exceeds 10 mg m^{-3}, it is reset to 10 to select the Q and R_{lim} values, which means that the threshold depends only on the solar angle.

For *MERIS*, the distributed product is the " normalized radiance reflectance", defined as

$$\rho_N(\theta_s, \theta_v, \Delta\varphi) = \pi L_w(\theta_s, \theta_v, \Delta\varphi) / E_d(0^+) \quad (9)$$

where $E_d(0^+)$ is the downward irradiance above the surface (0^+). Because $E_d(0^+)$ is not measured and instead is computed as in Eq. (1′), it results that ρ_N and $[L_w]_N$ are simply related through

$$\rho_N(\theta_s, \theta_v, \Delta\varphi) = \pi [L_w]_N(\theta_s, \theta_v, \Delta\varphi) / F_0 \quad (10)$$

or by using Eq. (3)

$$\rho_N(\theta_s, \theta_v, \Delta\varphi) = \pi R(\theta_s) \Re(\theta_v, W) / Q(\theta_s, \theta_v, \Delta\varphi, \mathrm{Chl}) \quad (11)$$

The introduction of $R_{\mathrm{lim}}(\lambda, \theta_s)$ (with $\lambda = 510$ or 560 nm for MERIS) into this equation allows the pixels belonging to case-2S waters to be identified, through an inequality similar to Eq. (8)

$$\rho_N(\theta_s, \theta_v \Delta\varphi, \lambda) > \rho_{N,\mathrm{lim}}(\theta_s, \theta_v, \Delta\varphi, \lambda)$$

where

$$\rho_{N,\mathrm{lim}}(\theta_s, \theta_v, \Delta\varphi\lambda) = \pi R_{\mathrm{lim}}(\lambda, \mathrm{Chl}, \theta_s) \Re(\theta_v, W) / Q(\theta_s, \theta_v, \Delta\varphi, \lambda, \mathrm{Chl}) \quad (12)$$

The resort to tabulated values for Q and R_{lim} is necessary to produce the needed limiting quantities, before testing the inequalities (Eqs. (8) and (12)). The appropriate lookup tables are available on the Internet (entries are θ_s, θ_v, $\Delta\varphi$, λ, Chl).

Actually, the above manipulations are greatly simplified, if "exactly" normalized radiometric quantities (Morel & Mueller, 2002) had already been produced. Recall that such exact quantities must be computed for a meaningful production of level-3 composites and also with the aim of merging coherent data sets from various satellites (recommendations in IOCCG, 2004). The exact normalization (ibid.) means that the bidirectional effects have been fully removed. This removal is obtained when $[L_w]_N$, or ρ_N, are given those particular values, $[L_w]_N^{ex}$, or ρ_N^{ex}, they would hypothetically exhibit, if θ_s, θ_v, and $\Delta\varphi$ were equal to 0. Briefly, this normalization requires a division (of $[L_w]_N$ and ρ_N) by the actual (i.e., angle-dependent) $\Re$ and Q values, then followed by a multiplication by $\Re_0$ (=0.529) and $Q_0(\mathrm{Chl}, \lambda)$. The quantities $\Re_0$ and Q_0 are the particular values corresponding to the idealized geometry of an observation made at nadir and when the sun is at zenith (and in absence of sun glint). In such a case, and because $\theta_s = 0$, the 2-D tables for the $R_{\mathrm{lim}}(\mathrm{Chl}, \theta_s = 0)$ values reduce for each wavelength to a polynomial function of (Chl), which describes the lower curves in Figs. 2 and 3A.

4.2. Examples of application

The same zone in the northern part of the Gulf of Mexico has been observed by the MERIS and the SeaWiFS sensors (on November 20, 2003).When processed in terms of chlorophyll concentration (Fig. 6a) by using algorithms strictly valid for

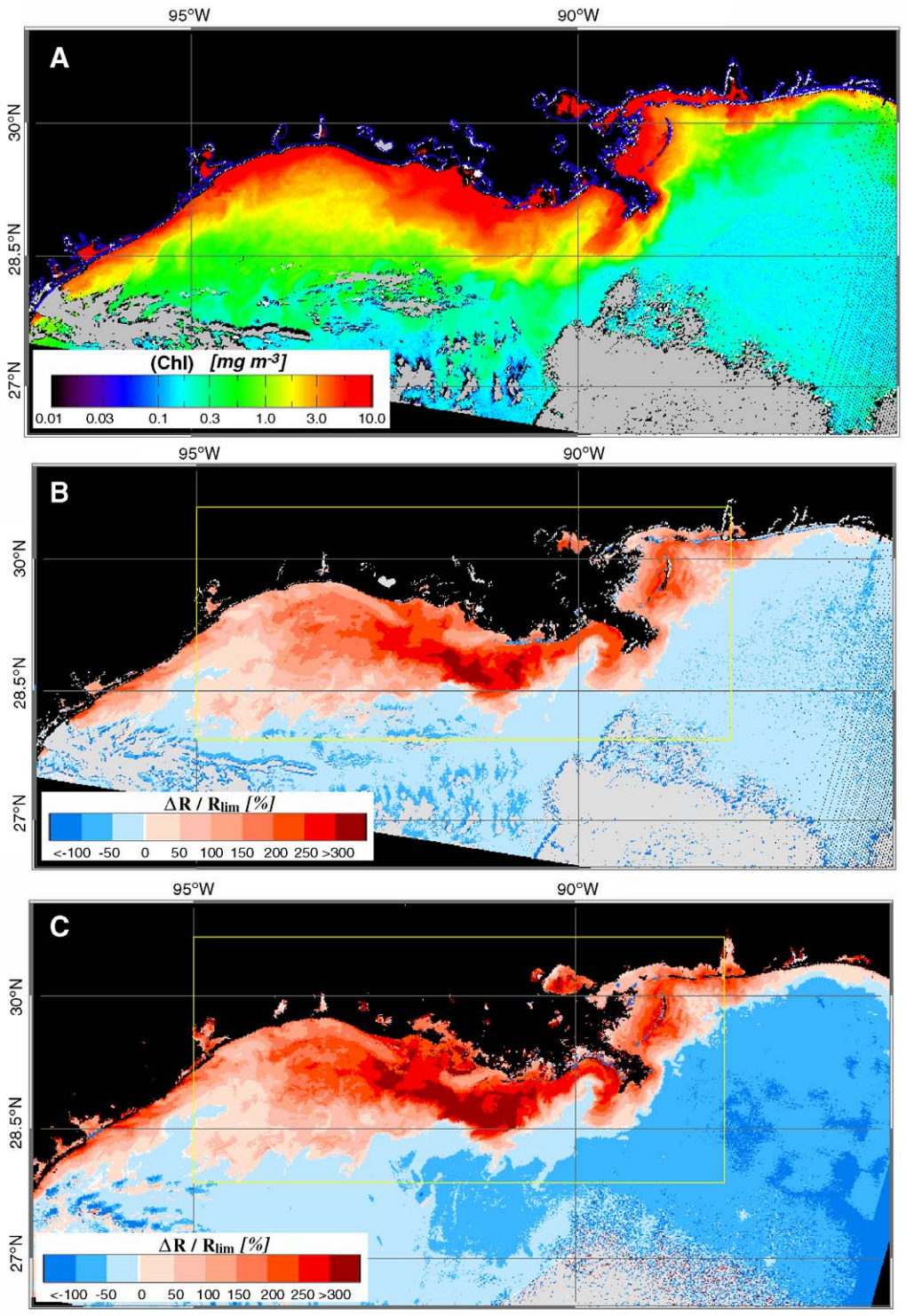

Fig. 6. Northern Gulf of Mexico, as seen on the 20th of November 2003 (solar time about noon for SeaWiFS and 10 am for MERIS). The images are geometrically rectified. (A) SeaWiFS data processed for (Chl) with the OC4V4 algorithm and by using SeaDAS 4.6 with the non-zero option for near-infrared radiance (Stumpf et al., 2003, algorithm); (B) processed in terms of relative differences (%) (Eq. (13)); (C) MERIS data processed in terms of relative differences (Eq. (12)). The yellow lines (namely the parallels 28.3°N and 30.5°N and meridians 88°W and 95°W) delimit the zone used to build the histograms in Fig. 7A and B.

case-1 waters, very high (Chl) levels (3–10 mg m^{-3} and beyond) appear along the coast and particular in the vicinity of the Mississippi and Alchafalaya deltas. The MERIS and SeaWiFS image return similar high (Chl) values in the same areas (Fig. 7A). They are questionable because of the interference with turbidity, which can be easily verified. For that, the two scenes are processed in terms of exactly normalized quantities by taking into account the geometry of each pixel (ρ_N^{ex} for MERIS and $[L_w]_N^{ex}$ for SeaWiFS); then, these quantities are compared to the upper limit values (Eqs. (8) and

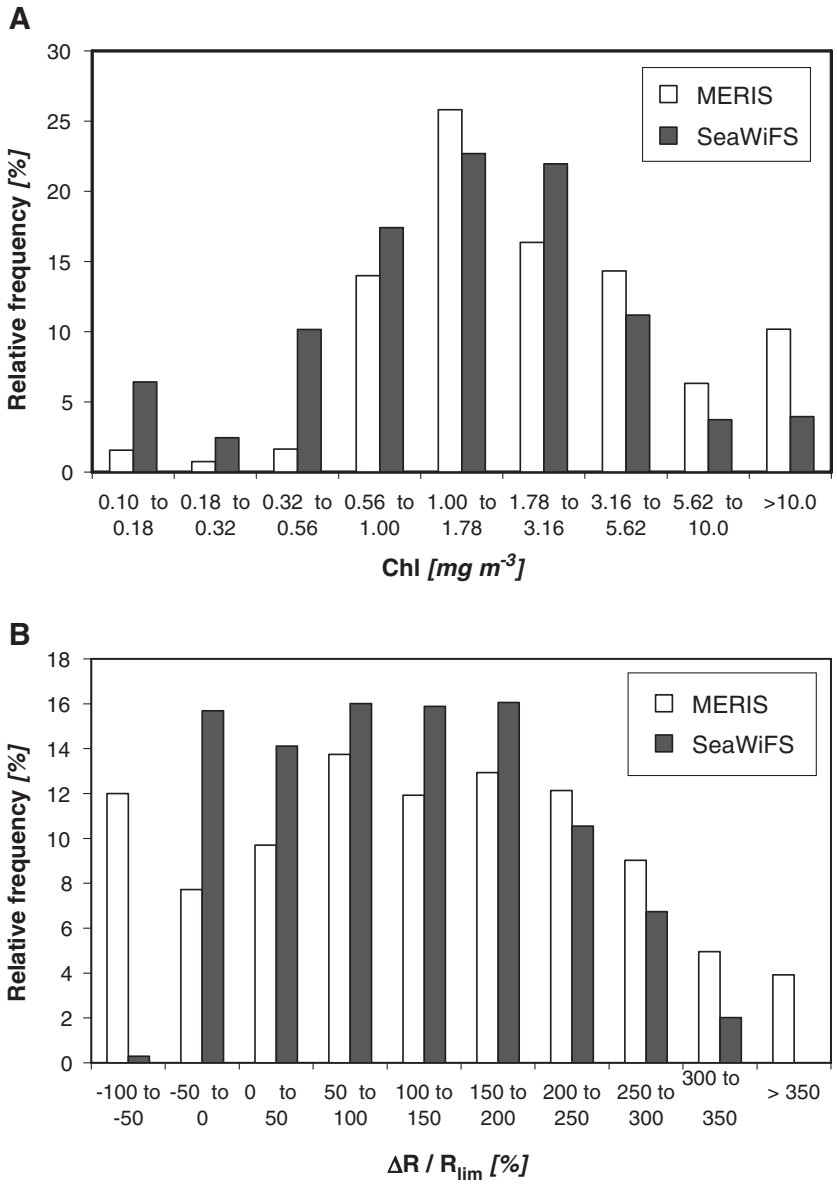

Fig. 7. (A) Histograms showing the frequency of occurrence of given (Chl) values in the SeaWiFS and MERIS imageries expressed as percent of the total number of the considered pixels (89,442 for MERIS and 58,580 for SeaWiFS) within the zone as delimited in Fig. 6. Note that the (Chl) values (about 82% of the total number), which are wrongly assessed in the turbid zones, are included in this histogram. (B) Frequency of occurrence of given relative differences $\Delta R/R_{\mathrm{lim}}$ (as %). The frequencies are expressed as percent of the total number of pixels within the same zone.

(12)). The quantities visualized on Fig. 6B and C are the relative differences (expressed as %) for the green wavelength (560 or 555 nm), namely

$$\Delta\rho_{\mathrm{N}}/\rho_{\mathrm{N,lim}} = 100(\rho_{\mathrm{N}} - \rho_{\mathrm{N,lim}})/\rho_{\mathrm{N,lim}} \tag{13}$$

and

$$\Delta[L_{\mathrm{w}}]_{\mathrm{N}}/[L_{\mathrm{w}}]_{\mathrm{N,lim}} = 100([L_{\mathrm{w}}]_{\mathrm{N}} - [L_{\mathrm{w}}]_{\mathrm{N,lim}})/[L_{\mathrm{w}}]_{\mathrm{N,lim}} \tag{13'}$$

Both these quantities are equal to

$$\Delta R/R_{\mathrm{lim}} = 100(R_{\mathrm{act}} - R_{\mathrm{lim}})/R_{\mathrm{lim}} \tag{14}$$

where R_{act} is the actual (i.e., the retrieved) reflectance. The color encoding is such that the positive relative differences (and the sediment load) are increasing from pale pink to red colors, whereas the blue colors are kept for negative differences (generally for case-1 waters, but yellow substance dominated waters could also enter into this category). The two sensors, and the proposed discrimination technique applied to both sources of data, lead to almost coinciding geographical patterns, as well as similar intensities of the turbidity signal. Other examples (not shown) confirm the reliability of the method (and the fair agreement between the two sensors, including their radiometric calibrations). The use of the criterion based on 510 nm, instead of 560 nm, leads to practically identical results (not shown). It must be noted also that inside highly turbid zones, filaments or patches of lower turbidity may appear. It is very plausible that locally enhanced yellow substance concentrations (which

optically thwart the scattering effect of sediment) are the cause of such features.

Identifying turbid waters by extending the above procedure to level-3 ocean color data is possible, with some manipulations and restrictions. If the level 2 images have been processed up to include the quantification of the radiance excess (the relative differences, as in Fig. 6), these excess can be merged to obtain a level-3 product and thus to provide temporally averaged maps of the turbid zones. Yet, if the level-3 composites result from level-2 scenes, which have been produced without identifying the turbid zones, the problem cannot be solved a posteriori. Indeed, the geometrical conditions (sun and viewing angles) needed to enter Eqs. (8) and (12) are lost in level-3, so that the accurate comparison with the threshold is no longer possible.

Normally, such an unfavorable situation must not occur. Indeed, the IOCCG (2004) recommendations stipulate that only the exactly normalized radiometric quantities can be merged within a level-3 composite. The "f/Q corrected" radiances (reprocessing 5.1) of SeaWiFS actually satisfy such a requirement. Therefore, the quantitative identification of sediment loaded waters becomes straightforward and identical whatever the level, which is considered (2 or 3). An example is provided for a monthly composite of the western European seas (Fig. 8). The well-known turbid zones (North Sea, Irish Sea, English channel, Mediterranean river plumes, etc.) are clearly delineated. Incidentally, the strongest negative differences are observed in the Baltic waters as a result of their high yellow substance concentrations.

5. Discussion and conclusion

Surprises sometimes occur with "turbid waters" detected far offshore in oceanic areas. Obviously, the presence of coccolithophorids or of abundant detached liths entails a reflectance shift similar to the one due to sediments. This real and natural phenomenon, however, has not to be confounded with some worrisome artifacts, which also may happen. Among those that have been identified during systematic processings, the following possible causes of reflectance enhancement can be cited:

(i) An insufficient rejection of areas still contaminated by sun glint. For instance, in the MERIS processing, "high glint" zones are rejected, whereas when the "medium glint" flag is raised, the processing is not stopped; these zones are most often detected as turbid; even at the periphery of medium glint areas, anomalously high reflectance are observed, meaning that the medium glint flag may be not severe enough;

(ii) The presence of unidentified white caps and bubbles. The similarity between the areas where high reflectances have been detected and the actual high wind pattern suggests that such a possibility exists (as observed in the Southern Ocean);

(iii) Some failure in the atmospheric correction process, particularly in presence of thin cirrus, or in the vicinity of clouds.

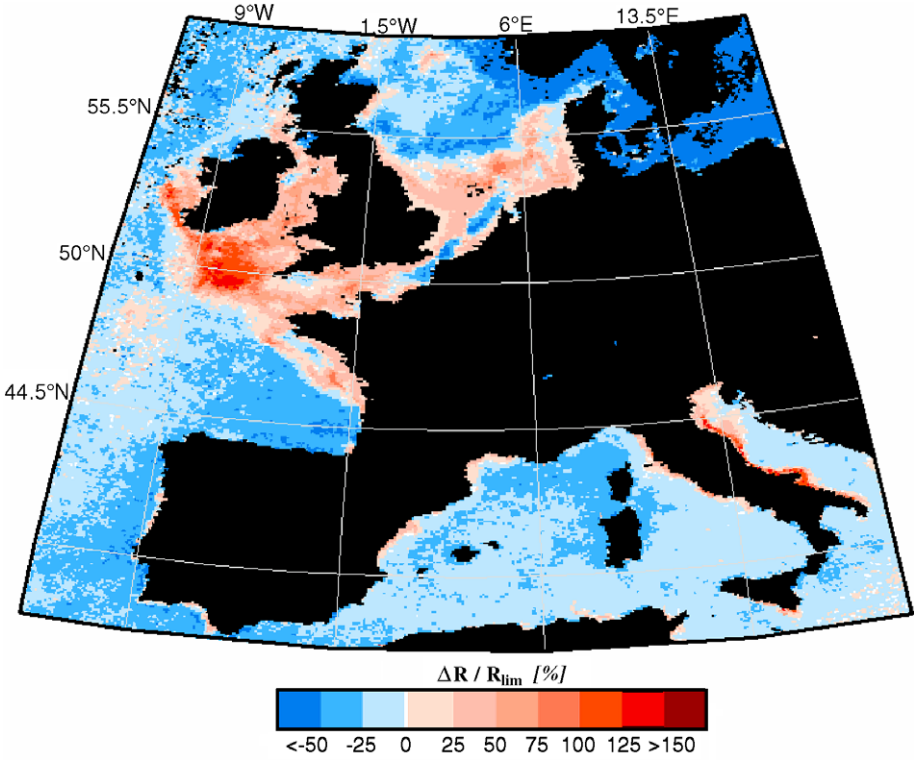

Fig. 8. Visualization of the turbid waters around Europe by applying Eq. (13) to the SeaWiFS monthly composite (March 2003) Level-3 as distributed by NASA (processed through version V5.1). The color encoding based on $\Delta R/R_{\mathrm{lim}}$ values is as for Fig. 6. According to a comment by one of the unknown referees, the negative $\Delta R/R_{\mathrm{lim}}$ values in the North Sea coincide with an intense bloom, which has occurred at this period in the zone in question.

When case-1 waters are near the coast, the artifacts described above may also occur. In addition, if the coast is highly reflective in the visible spectrum, the adjacency effects can induce an increase in marine reflectance (see, e.g., Santer & Schmechting, 2000), then wrongly interpreted as turbidity; shallow reflective bottom, as sandy bottom in atolls, produces a similar effect. In estuarine environment and inside turbid panache, the above artifacts cannot be easily detected if they occur, but other phenomena may impact the results, mainly

(i) If mixed case-2S–case-2Y waters, the presence of large amount of absorbing substances may prevent the reflectance from exceeding the prefixed threshold. With this respect, the criterion at 560 nm is preferable, as yellow substance (and other colored materials) exhibits an exponential decrease with increasing wavelength. The ambiguity is sometimes solved by using channels in the near IR, but such a choice involves another problem, that of the imperfect atmospheric correction in this spectral domain in presence of turbid reflective waters. The problem actually is also posed for the visible range.

(ii) Indeed, for turbid waters, the reflectance is not naught in the near IR. To account for that effect, a specific atmospheric correction (Moore et al., 1999) has been implemented in the MERIS processing, which starts with an identification of turbid waters. The corresponding flag is raised when $\rho_N(709) > 0.001$ (regardless of (Chl) and the sun position). Similarly, specific atmospheric correction schemes (also independent from (Chl) and bidirectional effects) have been developed for SeaWiFS (Lavender et al., 2005; Ruddick et al., 2000) and one of them is now implemented in the fourth SeaWiFS reprocessing (Stumpf et al., 2003). The non-zero marine signals in the near-infrared (not to be confounded with an aerosol contribution) are estimated via empirical relationships, before the atmospheric correction is carried out. It is out of the scope of the present paper to discuss the efficiency and compatibility of these corrections. The comparative histograms in Fig. 7B support the coherency of the results in terms of relative reflectance excess. The slight discrepancies regarding the frequency of occurrence (which originate from the difference in the near IR signal estimates and subsequent atmospheric correction) have a reduced impact as far as the geographical distribution of the turbid zones is concerned. Nonetheless, they may explain some subtle differences in Fig. 6B and C.

It is logical to try to interpret the excess of radiance (or of reflectance, Eq. (14)) as an index of the turbidity. A quantitative interpretation in terms of mass concentration of suspended sediment (e.g., as g m^{-3}) would be the desirable geophysical quantity. In coastal zones where empirical relationships between particle backscattering, or water-leaving radiance, and the sediment concentration have been (locally) documented, it is possible under some simplifying hypotheses to interpret the satellite imagery in terms of sediment concentration (see, e.g., Doxaran et al., 2002; Otero & Siegel, 2004; Salisbury et al., 2004; Warrick et al., 2004). An analytical and ubiquitous solution of this problem, however, is not easily within reach as briefly examined below.

The relative excess, $\Delta R/R_{lim}$ (Eq. (14)), or equivalently, the ratios $\Delta[L_w]_N/[L_w]_{N,lim}$ and $\Delta\rho_N/\rho_{N,lim}$ can be directly interpreted in terms of increase in backscattering under the simplifying assumption of linearity (Eq. (5)). By denoting $b_{b,sed}$ the additional backscattering due to the presence of sediment, the actual value, $b_{b,act}$, is the sum ($b_{b,lim}+b_{b,sed}$) and a straightforward calculation shows that

$$b_{b,sed}/b_{b,lim} = \Delta R/R_{lim} \quad (15)$$

The coefficient $b_{b,lim}$, which varies with (Chl), is already included in the model which has led to Figs. 2 and 3. Through Eq. (15), $b_{b,sed}$ can be assessed relatively to $b_{b,lim}$.

To go farther, two physical quantities are needed, namely the sediment backscattering efficiency $\tilde{b}_b$ to obtain b_{sed} through $b_{sed}=b_{b,sed}/\tilde{b}_b$, and then the mass-specific scattering coefficient b^*_{sed} (as $m^2\ g^{-1}$) to compute the (dry) sediment mass concentration, m_{sed} (g m^{-3}) through $m_{sed}=b_{sed}/b^*_{sed}$ Field experiments have not yet provided reliable $\tilde{b}_b$ values for sediment, even if for such refringent particles, it is reasonable to expect rather high (~2%) values (see Boss et al., 2004; Sullivan et al., 2005; Twardowski et al., 2001; Ulloa et al., 1994). Regarding b_{sed}*, many values have been published (ranging from 0.1 to more than 1 $m^2\ g^{-1}$; see, e.g., review in Babin et al., 2003a). The coexistence in varying proportions of inorganic and organic particles could explain this variability. A value of 0.5 $m^2\ g^{-1}$ for predominantly mineral particles seems plausible (ibid.), but may be locally inadequate. Assuming that the mass concentration has been assessed, it must be kept in mind that this information is restricted to the very near-surface layer (one or a few meters thick) "seen" by a remote sensor. In effect, the "penetration depth" (Gordon & McCluney, 1975) in such turbid waters is extremely reduced, so that a global estimate of the sediment vertical content (or of the outgoing sedimentary flux) is not feasible without external (hydrodynamical) information.

In summary, compared to previous, rather empirical techniques, the present method for identifying turbid case-2 waters is robust thanks to a more precise definition of the thresholds which account for the recent findings regarding the case-1 waters scattering properties. It is more accurate in the sense that the bidirectional effects, which are important, are taken into account and imbedded into the algorithm. Notwithstanding this, implementing this very simple method does not appreciably increase the processing time when producing level-2 or level-3 data. This method inevitably remains sensitive to any failure in the atmospheric correction scheme (accounting for non-zero radiance in the near-IR) and to the reliability of the retrieved water-leaving radiances. Nonetheless, its application will allow the zones where the chlorophyll retrieval is highly questionable to be identified. This tool also brings a valuable geochemical information about geographical extension and temporal variability of sediment plumes, and thence, on the frequency of occurrence of possible contamination, to the extent that pollutants drained from land are often co-occurring with the sediment transport.

Acknowledgements

The authors are deeply indebted to M. Babin, who made available the reflectance data in case-2 waters from the COAST/OOC campaigns, and to F. Fell for the processing of the radiometric data. We are also indebted to David Antoine, who made available the processed data from the Boussole site. A. Bricaud and M. Babin provided helpful and stimulating discussions on the first draft of this paper, and three anonymous referees helped by their constructive criticisms. We also thank B. Gentili for his efficient computer assistance. The financial supports from NASA and ESA to the Boussole activities, to the Biosope cruise, and to the (South African Marine and Coastal Management, MCM) Benguela cruise are duly acknowledged.

References

Ahn, Y. -H., Bricaud, A., & Morel, A. (1992). Light backscattering efficiency and related properties of some phytoplankters. *Deep-Sea Research. Part A, Oceanographic Research Papers*, *39*, 1835–1855.

Antoine, D., & Morel, A. (1999). A multiple scattering algorithm for atmospheric correction of remotely sensed ocean colour (MERIS instrument): Principle and implementation for atmospheres carrying various aerosols including absorbing ones. *International Journal of Remote Sensing*, *20*, 1875–1916.

Babin, M., Morel, A., Fournier-Sicre, V., Fell, F., & Stramski, D. (2003a). Light scattering properties of marine particles in coastal and open ocean waters as related to the particle mass concentration. *Limnology and Oceanography*, *48*, 843–859.

Babin, M., Stramski, D., Ferrari, G. M., Claustre, H., Bricaud, A., Obolenski, G., et al. (2003b). Variations in the light absorption coefficients of phytoplankton, non-algal particles, and dissolved organic matter in coastal waters around Europe. *Journal of Geophysical Research*, *108,* doi:10.1029/2001JC000882.

Boss, E., Pegau, W. S., Lee, M., Twardowski, M., Shybanov, E., Korotaev, G., et al. (2004). Particulate backscattering ratio at LEO 15 and its use to study particle composition and distribution. *Journal of Geophysical Research*, *109*, C01014, doi:10.1029/2002JC001514.

Bowers, D. G., Harker, G. E., & Stephan, B. (1996). Absorption spectra of inorganic particles in the Irish Sea and their relevance to remote sensing of chlorophyll. *International Journal of Remote Sensing*, *17*, 2449–2460.

Bricaud, A., & Morel, A. (1987). Atmospheric corrections and interpretation of marine radiances in CZCS imagery: Use of a reflectance model. *Oceanologica Acta*, 33–50.

Clarke, G. L., Ewing, G. C., & Lorenzen, C. J. (1970). Spectra of backscattered light from the sea obtained from aircraft as a measure of chlorophyll concentration. *Science*, 1119–1121.

Doxaran, D., Froidefond, J. -M., Lavender, S., & Castaing, P. (2002). Spectral signature of highly turbid waters: Application with SPOT data to quantify suspended particulate matter concentrations. *Remote Sensing of Environment*, *81*, 149–161.

Duntley, S. Q., Wilson, W. H., & Edgerton, C. F. (1974). Detection of ocean chlorophyll from earth orbit. *Scripps Institution of Oceanography*, 1.1–1.37 (SIO Ref 74-10).

Gordon, H. R. (2005). Normalized water-leaving radiance: Revisiting the influence of surface roughness. *Applied Optics*, *44*, 241–248.

Gordon, H. R., & Clark, D. K. (1981). Clear water radiances for atmospheric correction of Coastal Zone Color Scanner imagery. *Applied Optics*, *20*, 4174–4180.

Gordon, H. R., & McCluney, W. R. (1975). Estimation of the depth of sunlight penetration in the sea for remote sensing. *Applied Optics*, *14*, 413–416.

Gordon, H. R., & Morel, A. (1983). Remote assessment of ocean color for intrpretation of satellite visible imagery: A review. Lectures Notes on Coastal Estuarine Studies. 4, pp. 114, Springler-Verlag.

IOCCG (2000). Remote sensing of ocean colour in coastal, and other optically-complex, waters, Report Number 3. In V. Stuart (Ed.), *Reports of the international ocean-colour coordinating group* (pp. 1–139). Dartmouth, Nova Scotia, Canada.

IOCCG (2004). Guide to the creation and use of ocean colour level-3, binned data products, Report Number 4. In V. Stuart (Ed.), *Reports of the international ocean-colour coordinating group* (pp. 1–88). Dartmouth, Nova Scotia, Canada.

Lavender, S. J., Pinkerton, M. H., Moore, G. F., Aiken, J., & Blondeau-Patissier, D. (2005). Modification of the atmospheric correction of SeaWiFS ocean colour images over turbid waters. *Continental Shelf Research*, *25*, 539–555.

Loisel, H., & Morel, A. (1998). Light scattering and chlorophyll concentration in case 1 waters: A reexamination. *Limnology and Oceanography*, *43*, 847–858.

Loisel, H., & Morel, A. (2001). Non-isotropy of the upward radiance field in typical coastal (case-2) waters. *International Journal of Remote Sensing*, *22*, 275–295.

Maritorena, S., Siegel, D. A., & Peterson, A. (2002). Optimization of a semi-analytical ocean color model for global applications. *Applied Optics*, *41*, 2705–2714.

Moore, G. F., Aiken, J., & Lavender, S. (1999). The atmospheric correction of water colour and the quantitative retrieval of suspended matter in case II waters: Application to MERIS. *International Journal of Remote Sensing*, *20*, 1713–1733.

Morel, A. (1982). Optical properties and radiant energy in the waters of the Guinea dome and the Mauritanian upwelling area, in relation to primary production. Rapports et Procès-verbaux des Réunions, 180, 94-107. Conseil International pour l'Exploration de la Mer, Copenhague.

Morel, A. (1988). Optical modeling of the upper ocean in relation to its biogenous matter content. *Journal of Geophysical Research*, *93*, 10749–10768.

Morel, A., Antoine, D., & Gentili, B. (2002). Bidirectional reflectance of oceanic waters : Accounting for Raman emission and varying particle phase function. *Applied Optics*, *41*, 6289–6306.

Morel, A., & Gentili, B. (1996). Diffuse reflectance of oceanic waters: III. Implication of bidirectionality for remote sensing problems. *Applied Optics*, *37*, 4850–4862.

Morel, A., & Maritorena, S. (2001). Bio-optical properties of oceanic waters: A reappraisal. *Journal of Geophysical Research*, *106*, 7163–7180.

Morel, A., & Mueller, J. L. (2002). Normalized water-leaving radiance and remote sensing reflectance: Bidirectional reflectance and other factors. *Ocean Optics Protocols for satellite ocean color sensor validation*, *NASA/TM-2002-210004/Rev3-Vol2* (pp. 183–210).

Morel, A., & Prieur, L. (1977). Analysis of variations in oceran color. *Limnology and Oceanography*, *22*, 709–722.

O'Reilly, J. E., Maritorena, S., Mitchell, B. G., Siegel, D. A., Carder, K. L., Garver, S. A., et al. (1998). Ocean color algorithms for SeaWiFS. *Journal of Geophysical Research*, *103*, 24937–24953.

Otero, M. P., & Siegel, D. A. (2004). Spatial and temporal characteristics of sediment plumes and phytoplankton blooms in the Santa Barbara Channel. *Deep-Sea Research. Part II*, *51*, 1129–1149.

Preisendorfer, R. W. (1961). Application of radiative transfer theory to light measurement in the sea. *IUGG Monography*, *10*, 11–30.

Robinson, W. D., Franz, B. A., Patt, F. S., Bailey, S. W., & Werdell, P. J. (2003). Masks and flags updates. In S.B. Hooker, & E. R. Firestone (Eds.), *SeaWiFS Postlauch Technical Report Series*, *Chap.6, NASA/TM-2003-206892,vol 22* (pp. 34–40).

Roesler, C. S., Perry, M. J., & Carder, K. L. (1989). Modeling in situ phytoplankton absorption from total absorption spectra in productive inland waters. *Limnology and Oceanography*, *34*, 1510–1523.

Ruddick, K., Ovidio, F., & Rijkeboer, M. (2000). Atmospheric correction of SeaWiFS imagery for turbid and inland waters. *Applied Optics*, *39*, 897–912.

Salisbury, J. E., Campbell, J. W., Linder, E., Meeker, L. D., Müller-Karger, F. E., & Vörösmarty, C. J. (2004). On the seasonal correlation of surface particle fields with wind stress and Mississippi discharge in the northern Gulf of Mexico. *Deep-Sea Research. Part II*, *51*, 1187–1203.

Santer, R., & Schmechting, C. (2000). Adjency effects on water surfaces: Primary scattering approximation and sensitivity study. *Applied Optics*, *39*, 361–375.

Sullivan, J. M., Twardowski, M. S., Donaghay, P. L., & Freeman, S. A. (2005). Use of optical scattering to discriminate particle types in coastal waters. *Applied Optics*, *44*, 1667–1680.

Stramski, D., & Tegowski, J. (2001). Effects of intermittent entrainment of air bubbles by breaking wind waves on ocean reflectance and underwater light field. *Journal of Geophysical Research*, *106*, 31345–31360.

Stumpf, R. P., Arnone, R. A., Gould, R. W., Martinolich, P. M., & Ransibrahmanakul, V. (2003). A partially coupled ocean–atmosphere model for retrieval of water-leaving radiance from SeaWiFS in coastal waters, Chap. 9. In S. B. Hooker, & E. R. Firestone, (Eds.), *NASA/TM-2003-206892, vol 22* (pp. 51–59).

Stumpf, R. P., & Pennock, J. R. (1989). Calibration of a general optical equation for remote sensing of suspended sediments in moderately turbid estuary. *Journal of Geophysical Research*, *94*, 14363–14371.

Twardowski, M. S., Boss, E., Macdonald, J. B., Pegau, W. S., Barnard, A., & Zaneveld, J. R. V. (2001). A model for estimating bulk refractive index from the optical backscattering ratio and the implications for understanding particle composition in case I and case II waters. *Journal of Geophysical Research*, *106*, 14129–14142.

Ulloa, O., Sathyendranath, S., & Platt, T. (1994). Effect of particle-size distribution on the backscattering ratio in seawater. *Applied Optics*, *33*, 7070–7077.

Warrick, J. A., Mertes, L. A. K., Siegel, D. A., & Mackenzie, C. (2004). Estimating suspended sediment concentrations in turbid coastal waters of the Santa Barbara Channel with SeaWiFS. *International Journal of Remote Sensing*, *25*, 1995–2002.

Zhang, X., Lewis, M., Bissett, W. P., & Johnson, B. (2004). Optical influence of ship wakes. *Applied Optics*, *43*, 3122–3132.